



KING'S COLLEGE LONDON
DEPARTMENT OF PHYSICS

Feedback cooling of levitated nanoparticles using the polarization of light

Author:

Muhammad Haider

Supervisor:

Dr. James Millen

Co-Supervisor:

Dr. Maryam Nikkhou

A report submitted for the module of
7CCP4000 — MSci Project in Physics
January 17, 2024

Abstract

Levitated nanorods exhibit rotational and translational motion when subjected to polarized light. Modulating the light intensity and degree of polarization ellipticity gives control over this motion. This has led to the development of ultra-stable driven nanomechanical devices, with applications in the precise measurement of forces at the quantum limit. This report will explore the theory behind levitated optomechanics, introducing an FPGA-based implementation of a feedback mechanism that leads to cooling of the rotational degrees-of-freedom of a levitated nanorod. A protocol is provided to produce the required result.

Contents

1	Introduction	3
2	Background	4
2.1	Optical Trapping	4
2.2	Levitated Optomechanics	8
2.3	Rotational Optomechanics	10
2.4	Feedback Cooling	14
3	Method	18
3.1	FPGA	18
3.2	Red Pitaya	19
4	Experiment and Protocol	20
4.1	Red Pitaya High Bandwidth Averager	20
4.2	Red Pitaya PLL	20
4.3	Our Experiment	21
4.4	Expected Results and Analysis	25
5	Summary and Outlook	26
A	Appendix	28
A.1	Corrections to Polarizability	28
A.2	Gaussian Paraxial Approximation	28
A.3	Beam Power	28
A.4	Exact field distribution	28
A.5	Photon shot noise	29
A.6	A brief summary of Internal Temperature	29
A.7	Red Pitaya project	30
	Bibliography	33

1 Introduction

The effects of laser light on dielectric particles were first reported by Arthur Ashkin in 1970 [1]. This was achieved by using a TEM₀₀ mode beam of an argon laser focused through a solution of micro particles suspended within a liquid. It was shown that radiation pressure from the laser was able to impart a force on the particles along the direction of its propagation - the scattering force, \mathbf{F}_{scat} . Furthermore, particles with refractive index greater than the liquids were attracted to the lasers focus - through a gradient force, \mathbf{F}_{grad} . These principles were used by Ashkin and Dziedzic to realise the trapping (2D) of a 20 μm silica particle in free space [2] and later in a vacuum [3]. An electronic feedback system stabilising the particles centre-of-mass (c.o.m) motion was also introduced [4]. This utilised a novel linear feedback cooling mechanism, termed *cold damping*, which was able to cool a microparticle ($R= 1.5 \mu\text{m}$) to 1.5 mK. In the following years, laser traps found a range of uses in biophysics [5–9] and in quantum optics, for trapping and cooling of atoms [10, 11].

In 2010, Li *et al.* were able to conduct linear feedback cooling on levitated microparticles in a high vacuum and showed that due to limits set by recoil heating (observing ballistic Brownian motion), smaller nanoparticles will have to be employed for cooling to the quantum regime [12, 13]. In 2012, a novel *parametric* feedback cooling mechanism developed by Gieseler *et al.* was able to cool the c.o.m motion of a levitated nanoparticle ($R= 70 \text{ nm}$) to 50 mk [14]. This method used modulation of the laser intensity to change the stiffness of the trapping potential as a response to feedback of the c.o.m motion - working similarly to a damped harmonic oscillator. The rotational and torsional dynamics arising from trapped spherical nanoparticles have been studied in fluids [15, 16] and in free space [17, 18]. These types of interactions arise due to the transfer of *orbital* angular momentum from the lasers optical field to the levitated nanoparticle and offer applications in ultra precise measurement of forces at the quantum limit (as ground-state mechanical oscillators) [19–24]. This has been recently extended to include rotational control of cylinders and disks in a vacuum [25–27]. This is possible due to the transfer of *spin* angular momentum from the optical field. These dynamics were used to create an ultra-stable driven nanomechanical rotor that has torque sensitivities greater than 0.25 zNm [28].

The aim of this project is to show that an FPGA based device can be suitably used to control the feedback mechanism which leads to cooling of the rotational degrees-of-freedom (d.o.f) of a levitated nanorod.

2 Background

2.1 Optical Trapping

Consider a laser incident on a levitated nanoparticle. For a dielectric sphere of radius $R \gg \lambda$ (with λ being the optical trapping wavelength), a simple ray optics treatment may be applied. For $R \ll \lambda$, the particle may be treated as a dipole charge within an electric field, following the dipole approximation model. The following definitions are, in part, from [29, p. 456-].

The time-averaged force acting on the particle is given by:

$$\langle \mathbf{F} \rangle = \frac{\alpha'}{2} \sum_i \text{Re} \{ \underline{E}_i^* \nabla \underline{E}_i \} + \frac{\alpha''}{2} \sum_i \text{Im} \{ \underline{E}_i^* \nabla \underline{E}_i \} \quad (1)$$

where E_i is the complex incident electric field component ($\mathbf{E} = \text{Re}\{\mathbf{E}e^{i\omega t}\}$, with $\omega = 2\pi c/\lambda$ being the angular frequency of the field) and $\alpha = \alpha' + i\alpha''$ is the complex polarizability given by:

$$\alpha(\omega) = 4\pi\epsilon_0 R^3 \frac{\epsilon_r(\omega) - \epsilon_m(\omega)}{\epsilon_r(\omega) + 2\epsilon_m(\omega)} \quad (2)$$

with ϵ_r being the relative permittivity, ϵ_m being the permittivity of the surrounding material (in a vacuum, $\epsilon_m = 1$) and ϵ_0 is the permittivity of free space. In reality, due to radiative losses there are some corrections to the polarizability (see A.1)

The real part of the polarizability, α' , determines the optical potential and the first term from equation 1 is referred to as the gradient force, as it may be written:

$$\langle \mathbf{F}_{\text{grad}} \rangle = \frac{\alpha'}{2} \langle \nabla \mathbf{E}^2 \rangle = \frac{\alpha'}{2c\epsilon_0} \nabla I \quad (3)$$

where I is the intensity,

$$I = \text{cn} \epsilon_0 \frac{|\mathbf{E}|^2}{2} \quad (4)$$

with n being the complex refractive index of the particle, related to permittivity through $\epsilon_r(\omega) = n(\omega)^2$.

The sign of the gradient force changes as the particle moves past the focus of the laser and in consequence, the particle is attracted to the region of highest intensity with a predictable trapping frequency and potential. Since $\nabla \times \langle \mathbf{F}_{\text{grad}} \rangle = 0$, this is a conservative force and no work is done on the particle. The gradient force does not involve any transfer of momentum, instead the mechanism is attributed to forward-Rayleigh scattering and the relevant energy transitions are found using second-order perturbation theory [30].

The imaginary part of the polarizability, α'' , determines the optical absorption and the second term in equation 1 is referred to as the scattering force:

$$\langle \mathbf{F}_{\text{scat}} \rangle = \frac{\alpha'' \omega}{\varepsilon_0 c^2} \langle \mathbf{S} \rangle - i \frac{\alpha''}{4} [\nabla \times (\mathbf{E} \times \mathbf{E}^*)] \quad (5)$$

where $\langle \mathbf{S} \rangle$ is the time averaged Poynting vector given by:

$$\langle \mathbf{S} \rangle = \frac{|\mathbf{E}|^2}{2\varepsilon_0 c}, \quad (6)$$

and the second term is the force associated with the spin density of the light field which is relevant in fields with non-uniform helicities [31]. The scattering force may be written (by considering photon flux under conservation of momentum) as:

$$\langle \mathbf{F}_{\text{scat}} \rangle = \frac{n\sigma_s}{c} \langle \mathbf{S} \rangle, \quad (7)$$

where σ_s is the Rayleigh scattering cross-section given by [32, p. 171]:

$$\sigma_s = \frac{128\pi^5}{3} \cdot \frac{\alpha^2}{\lambda^4} \quad (8)$$

Finally, substituting equations 4, 6, 8 into equation 7, the scattering force may be written as:

$$\mathbf{F}_{\text{scat}} = \frac{128\pi^5 n}{3c} \cdot \frac{R^6}{\lambda^4} \left(\frac{\varepsilon_r(\omega) - 1}{\varepsilon_r(\omega) + 2} \right)^2 I \hat{z} \quad (9)$$

Since $\nabla \times \langle \mathbf{F}_{\text{scat}} \rangle$ is non vanishing, the scattering force is non-conservative and is able to do work on the particle. This force arises due to the transfer of linear momentum from the electromagnetic field radiation to the particle. This is achieved either through direct absorption of incident photons, or a change in the direction of the photons due to interaction with the particle (non-forward scattering) [30]. The former leads to motion along the direction of the beam through the conservation of momentum, whilst the latter leads to motion along the axial direction, \hat{z} , of the trap - working against the gradient force. Furthermore, it is seen that the gradient force scales with R^3 while the scattering force scales with R^6 - meaning larger particles experience stronger scattering forces. Through the fraction $\frac{\mathbf{F}_{\text{scat}}}{\mathbf{F}_{\text{grad}}} > 1$ (scattering force dominates gradient force and the particle is forced away from the beams focus), the following condition arises:

$$R > \sqrt[3]{\frac{3\lambda^4}{16\pi^4} \frac{\nabla I}{I} \left(\frac{\varepsilon_r(\omega) - 1}{\varepsilon_r(\omega) + 2} \right)} \quad (10)$$

For particles with radius fulfilling this condition, the scattering force dominates. In general, it is found that traps facilitating microparticles need the additions of gravity [33], two counter-propagating beams [34] or a standing wave [35], to compensate for the scattering force. Whereas for nanoparticles ($R \sim 580$ nm), the scattering force is much weaker

than the gradient and the particle remains trapped within the lasers focus. If displacement of the particle remains small with respect to (w.r.t) the lasers width parameters, motion can be restricted to a harmonic potential well. An overview of the scattering and gradient forces involved for micro/ nanoparticles is given in figure 1.

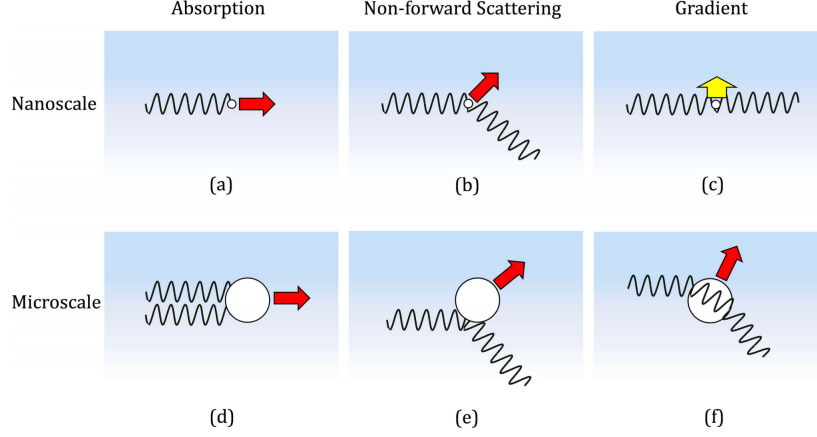


Figure 1: Different kinds of laser-induced forces on nano and microparticles. (a), (d) absorption and (b), (e) non forward scattering is from the direct transfer of momentum from photons. (c), (f) The gradient force is directed towards the fields highest intensity region (laser intensity profile indicated by blue gradient). From Ref. [30]

The laser being used has a Gaussian function intensity profile. The shape of the Gaussian beam of a given wavelength is governed by the radius of the field amplitude, or the beam waist:

$$w(z) = w_0 \sqrt{1 + \left(\frac{z}{z_R}\right)^2} \quad (11)$$

where w_0 is the beam waist at the origin, z is the axial distance from the origin and z_R is the Rayleigh length

$$z_R = \frac{\pi w_0^2}{\lambda}, \quad (12)$$

which determines the depth of focus. Another useful parameter to define is the radius of curvature of the beam waist:

$$R(z) = z \left[1 + \left(\frac{z}{z_R}\right)^2 \right] \quad (13)$$

It is assumed that the Gaussian has a beam waist that is large enough (in relation to the particle) that higher order corrections do not need to be considered and the paraxial approximation (see A.2) has been applied.

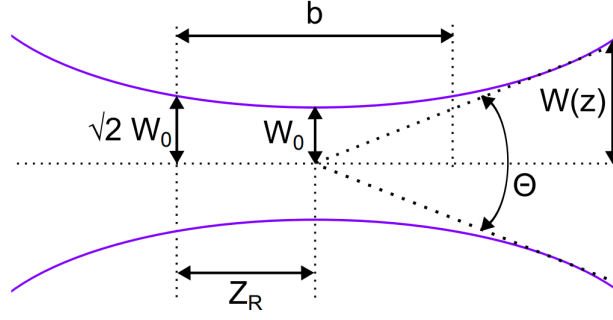


Figure 2: Gaussian beam parameters. θ is the total angular spread, b is the depth of focus ($2b = z_R$). and $w_0 = \sqrt{2}z_R$ ($w_0 = 2/k\theta_{max}$). From Ref. [36]

The incident complex electric field is now given by:

$$\mathbf{E}_{\text{inc}}(\mathbf{r}, t) = \mathbf{E}_0 \exp\left(-\frac{x^2 + y^2}{w_0^2}\right) \quad (14)$$

where $\mathbf{r} = (x, y, z)^T$ and $|\mathbf{E}_0| = \sqrt{4P/(c_0\epsilon_0\pi w_0^2)}$, with P being the optical power of the beam (see A.3). After this incident field has gone through a focusing lens, the resulting Gaussian profile becomes [14, p. 22]:

$$\mathbf{E}(\mathbf{r}) = \mathbf{E}_0 \left(\frac{z^2}{w_{z0}^2} + 1\right)^{-\frac{1}{2}} \exp\left[-\frac{\frac{x^2}{w_{x0}^2} + \frac{y^2}{w_{y0}^2}}{\frac{z^2}{w_{z0}^2} + 1} + i\phi(\mathbf{r})\right] \quad (15)$$

where

$$\phi(\mathbf{r}) = kz - \arctan\left(\frac{z}{w_{z0}}\right) + \frac{k(x^2 + y^2)}{2z\left(1 + \frac{w_{z0}^2}{z^2}\right)} \quad (16)$$

with k being the wavevector ($k = \frac{2\pi}{\lambda}$) and w_{i0} being the beam waist along the x, y, z axis. The intensity of the laser is found to have the following relation [36]:

$$\begin{aligned} I(r_{\text{rad}}, z) &= \frac{|\mathbf{E} \times \mathbf{H}^*|}{2} = \frac{|\mathbf{E}(r_{\text{rad}}, z)|^2}{2\eta} \\ &= I_0 \left(\frac{W_0}{W(z)}\right) \exp\left(\frac{-2r_{\text{rad}}^2}{W(z)^2}\right) \end{aligned} \quad (17)$$

where $r_{\text{rad}} = \sqrt{x^2 + y^2}$ is the radial distance, \mathbf{H}^* is the complex magnetic field (along \hat{y}) and η is the impedance of the medium.

2.2 Levitated Optomechanics

By considering the energy of a dipole within an electric field, $U_{opt} = -\mathbf{p} \cdot \mathbf{E}$ (where \mathbf{p} is the dipole moment) and using the relation $\mathbf{p} = \alpha \mathbf{E}$, we arrive at an expression for the trapping potential:

$$U_{opt}(\mathbf{q}) = -\frac{\alpha'}{4} |\mathbf{E}^2(\mathbf{q})| = -\frac{\alpha'}{2c\epsilon_0} I(\mathbf{q}) \quad (18)$$

where $q \in \{x, y, z\}$ is the position of the particle. Substituting the Gaussian wave profile (equation 15) and expanding the optical potential up to the fourth order gives [37]:

$$U_{opt}(\mathbf{q}) = U_0 \left[-1 + \frac{2q_x^2}{w_{x0}^2} + \frac{2q_y^2}{w_{y0}^2} + \frac{q_z^2}{w_{z0}^2} - \frac{2q_x^4}{w_{x0}^4} - \frac{2q_y^4}{w_{y0}^4} - \frac{q_z^4}{w_{z0}^4} - \frac{4q_x^2 q_y^2}{w_{x0}^2 w_{y0}^2} - \frac{4q_x^2 q_z^2}{w_{x0}^2 w_{z0}^2} - \frac{4q_y^2 q_z^2}{w_{y0}^2 w_{z0}^2} \right] \quad (19)$$

where $U_0 = \alpha' E_0^2 / 4 = \alpha' I_0 / 2c\epsilon_0$ is the trap depth, q_i is the particle position and w_{i0} is the beam waist (at the origin). It should be noted that these are not the simple paraxial expressions stated previously, they are free parameters made to fit an exact solution of the field distribution (see A.4). For $q_i \ll w_{i0}$, U_{opt} can be approximated to be harmonic and the potential acts as a linear spring:

$$\langle F_{grad,q} \rangle = -k_q q \quad q \in \{x, y, z\} \quad (20)$$

with trap stiffness:

$$k_a = \frac{\alpha' E_0^2}{w_{a0}^2}, \quad k_z = \frac{\alpha' E_0^2}{2w_{z0}^2} \quad a \in \{x, y\} \quad (21)$$

For large displacements, the quartic terms from equation 19 start to become significant and additional parameters in the potential are obtained:

$$\xi_q = -\frac{2}{w_{q0}^2} \quad (22)$$

These are the Duffing parameters [38–40] and are responsible for nonlinearities in the harmonic potential. The equation for the trapped particles centre-of-mass (c.o.m) motion is given by:

$$\ddot{q}(t) + \Gamma_0 \dot{q}(t) + \Omega_0^2 q(t) = \frac{1}{m} [F_{fluct}(t) + \Sigma F_i(t)] \quad (23)$$

where m is the mass of the trapped particle, $\Omega_0 = \sqrt{k_q/m}$ is the mechanical oscillation frequency, Γ_0 is the total momentum damping rate, F_{fluct} is the total fluctuating force and F_i is the sum of all other forces. Nonlinear contributions may be neglected if [41]:

$$\frac{3k_B T_0}{w_{q0}^2 \Gamma_0 \Omega_0 m} \ll 1 \quad (24)$$

where k_B is Boltzmann's constant and T_0 is the effective bath temperature (temperature at c.o.m).

F_{fluct} is a random Langevin which may be defined through the fluctuation-dissipation theorem [14]:

$$\langle F_{fluct}(t) F_{fluct}(t') \rangle = 2m\Gamma_0 k_B T_0 \delta(t - t') \quad (25)$$

where δ is the Dirac delta function. At low-vacuum conditions, Γ_0 is dominated by collisions with the surrounding gas, such that $\Gamma_0 \approx \Gamma_{gas}$. Through the kinetic gas theory, the gas damping rate for a spherical particle is given by [42]:

$$\Gamma_{gas} = \frac{6\pi\eta_{gas} R}{m} \frac{0.619}{0.619 + Kn} (1 + c_K) \stackrel{Kn \gg 1}{\approx} \frac{8}{3} \sqrt{\frac{2m_{gas}}{\pi k_B T_{im}}} R^2 P_{gas} \quad (26)$$

where $Kn = l_{gas}/R$ is the Knudsen number (l_{gas} is the mean free path and R is the radius of the trapped particle), η_{gas} is the dynamic viscosity of the background gas ($= 18.27 \times 10^{-6}$ kgms $^{-1}$ for air), $c_K = 0.31Kn / (0.785 + 1.152Kn + Kn^2)$, T_{im} is the temperature of the impinging gas (see A.6) and P_{gas} is the pressure of the gas. The mean free path is given by [43]:

$$\ell = \frac{\eta_{gas}}{P_{gas}} \sqrt{\frac{\pi N_A k_B T_{im}}{2M_{gas}}} \quad (27)$$

where M_{gas} is the molar mass ($= 28.97 \times 10^{-3}$ kg/mol for air) and N_A is the Avogadro constant. As P_{gas} decreases to low vacuum conditions, l_{gas} increases such that $Kn \gg 1$ is valid. This transition to the *Knudsen regime* occurs at $P_{gas} \approx 54.4$ mbar/ $R(\mu m)$ [41]. In reality, there are other sources of damping such as radiation damping and photon shot noise [44] (discussed briefly in A.5).

Motion in the harmonic potential is difficult to analyse due to F_{fluct} , it may be characterised by the power spectral density (PSD) and can be derived from equation 23 by application of the Wiener-Khinchin theorem [14]:

$$\begin{aligned} S_{qq}(\Omega) &= \int_{-\infty}^{\infty} \langle q(t) q(t - t') \rangle e^{-i\Omega t'} dt' \\ &= \frac{\Gamma_0 k_B T_0 / (\pi m)}{(\Omega_0^2 - \Omega^2)^2 + \Omega^2 \Gamma_0^2} \end{aligned} \quad (28)$$

S_{qq} is acquired experimentally and the extraction of the c.o.m temperature is possible after fitting to the data. Non-linear dynamics will not be considered within the context of this report.

2.3 Rotational Optomechanics

When considering the rotational aspects of optical levitation one must consider the optical torque. The radiation force (non-forward scattering and absorption) can involve the transfer of angular momentum which results in: the spin of the particle along its axis (spin angular momentum) and orbit around a central point (orbital angular momentum). The gradient force results in a torque that causes cylindrical particles to align in certain directions within the trapping potential. Torsional motion leads to a change in the moment of inertia, I . This corresponds to very high torsional frequencies (compared to vibrational) which is desirable for quantum optomechanics [41]. Having access to more *liberation* (replacing torsional) modes hints at greater torque sensitivity [28, 45].

Torque due to gradient force:

For a cylindrical particle with polarizability α_{\parallel} , along the axial direction, and α_{\perp} along the transverse direction, there is a nanoscale torque [30]:

$$\boldsymbol{\tau} = (\alpha_{\perp} - \alpha_{\parallel}) \left(E_y \hat{\mathbf{x}} - E_x \hat{\mathbf{j}} \right) E_z \quad (29)$$

which aligns its axis of symmetry with the polarization plane (perpendicular to the direction of propagation of the beam). This arises when there is **linearly polarized** light. Spherical particles have the same polarizability in all directions and do not experience this torque.

Torque due to spin angular momentum:

Spin angular momentum is able to be transferred to anisotropic particles (nonrods) through optical scattering (from radiation force). This arises when there is **circularly polarized** light. The resulting torque acts on angle α [27]:

$$N_{\alpha} = \frac{P_{\text{tot}} \Delta\chi \ell^2 d^4 k^3}{48 c w_0^2} [\Delta\chi \eta_1(k\ell) + \chi_{\perp} \eta_2(k\ell)] \quad (30)$$

where where d is the diameter of the cylinder, ℓ is the cylinders length, $\Delta\chi = (\epsilon_r - 1)^2 / (\epsilon_r + 1)$ is the susceptibility anisotropy, χ_{\perp} is the susceptibility perpendicular to the rods symmetry axis and

$$\begin{aligned} \eta_1(k\ell) &= \frac{3}{4} \int_{-1}^1 d\xi (1 - \xi^2) \text{sinc}^2\left(\frac{k\ell\xi}{2}\right) \\ \eta_2(k\ell) &= \frac{3}{8} \int_{-1}^1 d\xi (1 - 3\xi^2) \text{sinc}^2\left(\frac{k\ell\xi}{2}\right). \end{aligned} \quad (31)$$

The third type of torque, due to orbital angular momentum, arises for any plane polarized light and occurs predominantly for spherical particles. This is associated with the non-forward scattering radiation force [30].

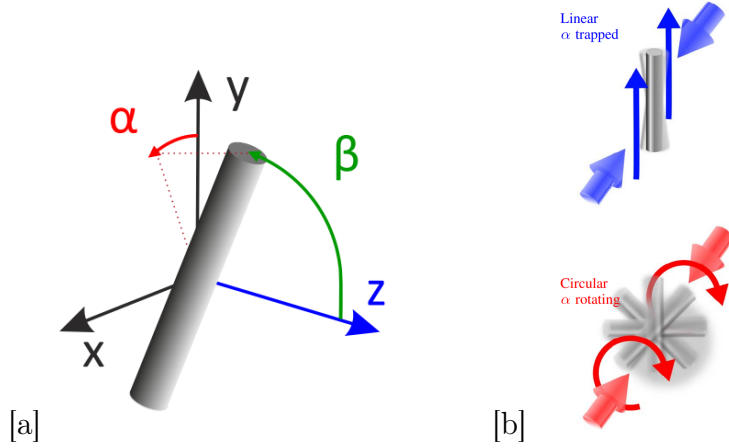


Figure 3: [a] Rotating cylinder. α is the angle between the x-axis and the projection onto the x-y plane. β is the angle between the cylinders symmetrical axis and the z-axis. From Ref. [41] [b] The two different types of rotations arising from linearly polarized light (top) and circularly polarized light (bottom). From Ref. [27]

Trapping frequencies (when the laser has co-linear polarization) for each d.o.f are calculated as [26]:

$$\begin{aligned}
 f_{x,y} &= \frac{1}{2\pi} \sqrt{\frac{8P_{\text{tot}}\chi_{\parallel}}{\pi\rho c w_0^4}}, \quad f_z = \frac{1}{2\pi} \sqrt{\frac{4P_{\text{tot}}\chi_{\parallel}k^2}{\pi\rho c w_0^2}} \\
 f_{\beta} &= \frac{1}{2\pi} \sqrt{\frac{48P_{\text{tot}}\chi_{\parallel}}{\pi\rho c w_0^2\ell^2} \left(\frac{\Delta\chi}{\chi_{\parallel}} + \frac{(k\ell)^2}{12} \right)} \\
 f_{\alpha} &= \frac{1}{2\pi} \sqrt{\frac{48P_{\text{tot}}\Delta\chi}{\pi\rho c w_0^2\ell^2}}
 \end{aligned} \tag{32}$$

where $\chi_{\parallel} = \varepsilon_r - 1$ is the susceptibility along the cylinders symmetrical axis, w_0 is the trapping waist radius, P_{tot} is the total power of the laser beam and ρ is the particles density. At this trapping frequency, the cylinder nanoparticle becomes trapped in all d.o.f.

Collisions with background gas particles leads to damping of rotational motion. The rotational damping rate for a sphere is found to be [41]:

$$\Gamma_{\text{rot}}^{\text{sph}} = \frac{10\alpha_C P_{\text{gas}} R^2}{3m} \sqrt{\frac{2\pi m_{\text{gas}}}{k_B T_{\text{env}}}} \tag{33}$$

where T_{env} is the temperature of the environment, T_{gas} is that of the gas and α_C is the energy accommodation coefficient given by:

$$\alpha_C = \frac{T_{\text{em}} - T_{\text{im}}}{T_{\text{int}} - T_{\text{im}}} \tag{34}$$

with T_{em} being the temperature of the emitted gas particles and T_{int} being the internal/bulk temperature of the trapped nanoparticle. This quantity arises when considering some

thermodynamic properties (see A.6).

The cylindrical rotational damping is given by [41]:

$$\Gamma_{\text{rot}}^{\text{cyl}} = \frac{P_{\text{gas}} d \ell}{m} \sqrt{\frac{2\pi m_{\text{gas}}}{k_B T_{\text{gas}}}} \left(2 - \frac{1}{2} \alpha_C + \frac{\pi}{4} \alpha_C \right) \quad (35)$$

The maximum rotational frequency at the steady-state is found by balancing equations 30 and 35 [27]:

$$f_{\alpha, \text{max}} = \frac{N_{\alpha}}{2\pi I \Gamma} \quad (36)$$

where $I = M\ell^2/12$ is the cylinders moment of inertia. Rotational and translational (from harmonic potential) motion are fundamentally different as rotational motion is associated with non-linearity's w.r.t the dynamic variables [46]. The consequent PSD is found by measurement of the scattered light data (more detail in next section) [47]:

$$\text{PSD}(\Omega) = C_d^2 \frac{2k_B T_0}{m_d} \frac{\Gamma_d}{(\Omega_d^2 - \Omega^2)^2 + \Omega^2 \Gamma_d^2} \quad (37)$$

where d is the degree of freedom (x, y, z, α, β) , m_d is the particles mass, Ω_d is the trapping frequency, Γ_d is the angular momentum damping rate and C_d is the calibration between the measured signal and the actual motion of the nanoparticle.

By adjusting the polarization of the incident laser, the rotational motion of the nanorods can be studied. The main result is summarised in figure 4.

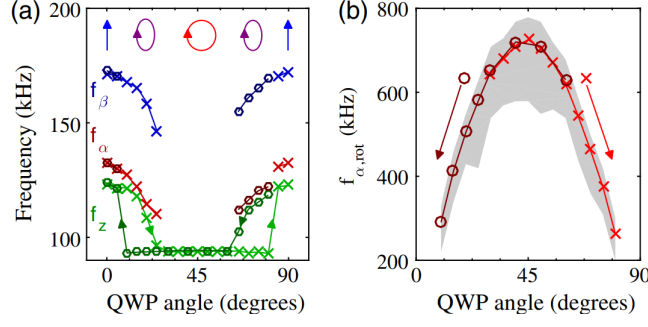


Figure 4: Starting from linear polarization along \hat{y} , increasing ellipticity by performing a quarter-wave-plate (QWP) operation. (a) All trapping frequencies are reduced as ellipticity is increased due to reduced trap depth. As QWP angle approaches 45° (circular polarization), $f_{\alpha,rot}$ is driven to the max (b) and $f_{\alpha,\beta}$ vanishes. From Ref. [27]

As ellipticity is initially increased, all trapping frequencies are reduced due to reduced trap depth. At 30° , the light starts to become circularly polarized and rotations start in the α direction. For this reason the $f_{\alpha,\beta}$ trapping frequencies disappear (as they have begun rotating). f_z is stabilised at a frequency of ~ 94 kHz. Rotating beyond 45° , the rod becomes trapped again at 90° (30° later than would be expected from symmetry). This discrepancy is attributed to the anisotropy of the susceptibility tensor. When a nanorod is trapped by linearly polarized light, it is in a trap depth related to χ_{\parallel} . When circularly polarized light is incident on the nanorod, its trap depth is related to $(\chi_{\parallel} + \chi_{\perp})/2$ - the average of the susceptibility over the rotational plane (a smaller value). This corresponds to a smaller torque - a trapped nanorod requires a larger torque to start rotating than an already rotating one.

2.4 Feedback Cooling

Before commencing any feedback cooling, the particles positional data must be found. This is done by analysing the field scattered by the trapped particle. Calibration of the measured signal allows the particles position to be extracted. For a nanosphere (following dipole approximation model), the power of the scattered field is given by [41]:

$$P_{\text{scat}} = |\alpha|^2 k_L^4 I_{\text{opt}} / 6\pi\epsilon_0^2 \quad (38)$$

where I_{opt} is the local intensity (of the trapped particles position) and varies depending on the particles position within the beams intensity profile (calculated here [48]).

Using a tightly focused beam (Gaussian intensity profile) produces greater position resolution and using standing waves increases resolution along the axial direction (\hat{z}) [41]. The scattered photons are detected by using a photodetector [49] or a multi-mode fibre (MMF) [25, 27]. The different degrees-of-freedom of position data can be also obtained separately by using a quadrant photodiode (QPD) [24]. Next the detected signals are calibrated by analysing the PSD (assuming thermal equilibria is reached and motion is perfectly harmonic).

The simplest way the trapped particle may be cooled is by *cold damping*. This works by introducing a new term in the equation of motion:

$$\ddot{q}(t) + \Gamma_0 \dot{q}(t) + \Omega_0^2 q(t) = \frac{1}{m} F_{\text{fluct}}(t) + u_{fb}(t) \quad (39)$$

where $u_{fb}(t) = G_{\dot{q}} \dot{q}(t)$, with $G_{\dot{q}}$ being some optimized gain. Another feedback term which may be employed is $u_{fb}(t) = G_q q(t) + G_{\dot{q}} \dot{q}(t)$ which results in a faster cooling rate but not a lower c.o.m temperature. This type of adaptive feedback control scheme was used by Ashkin as mentioned in the introduction (R=1.5 μm to 1.5 mK) [4].

Parametric feedback cooling was first presented in 2012 by Giesler *et al.* (R=70 nm to 50 mK) [50]. This method works by modulating the optical potentials depth such that the trap stiffness increases when the particle climbs the potential well. This reduces the particles average internal kinetic energy and hence decreases its c.o.m temperature. The modulation acts at twice the trap frequency (and so is twice as fast as "cold damping"), applied at a relative phase to the particles motion. Since the intensity of the laser is related to the trapping potential (equation 18) and consequently to the trap stiffness ($U = \frac{1}{2} k_q^2$ for a perfect spring), modulation of the lasers intensity allows control of the feedback amplitude.

The new equation of motion becomes:

$$\ddot{q}(t) + \Gamma_0 \dot{q}(t) + \Omega_0^2 q(t) = \frac{1}{m} (F_{\text{fluct}}(t) + F_{fb}(t)) \quad (40)$$

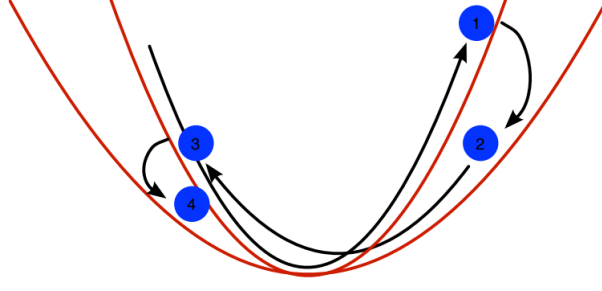


Figure 5: Trap Modulation. Motion of 1 is before parametric feedback has been activated. Then between 2 and 3 as the particle moves away from the centre, trap stiffness is increased and the particle loses energy. At 4, the modulation is repeated. From Ref. [14]

where the additional force is $F_{fb}(t) = k_{fb}(t)q(t)$. The modulating stiffness given by

$$k_{fb}(t) = k_q \eta \sin(2\Omega_0 t + \phi) \quad (41)$$

with ϕ being the relative phase of the particles motion to the trap frequency, η is the modulation depth, $\eta = I_{fb}/I_0$ with I_0 being the intensity of the laser before feedback and I_{fb} is the amplitude of the feedback modulation. The total trap stiffness now becomes $k(t) = k_q + k_q \eta \sin(2\Omega_0 t + \phi)$.

This modulating feedback results in a slight shift in the total momentum damping rate by $\delta\Gamma$ and the mechanical oscillation frequency by $\delta\Omega$. The PSD becomes:

$$S_{qq}(\Omega) = \frac{\Gamma_0 k_B T_0 / (\pi m)}{([\Omega_0 + \delta\Omega]^2 - \Omega^2)^2 + \Omega^2 [\Gamma_0 + \delta\Gamma]^2} \quad (42)$$

The following definitions are from [14]. By integrating both sides over Ω , the mean square displacement is found:

$$\begin{aligned} \langle q^2 \rangle &= \int_0^\infty S_{qq}(\omega) d\omega \\ &= \frac{\Gamma_0 k_B T_0}{m} \frac{1}{\omega_0^2 (\Gamma_0 + \delta\Gamma)} \end{aligned} \quad (43)$$

Through the equipartition theorem, $k_B T_{\text{eff}} = m (\Omega_0 + \delta\Omega)^2 \langle q^2 \rangle$. For the limit $\delta\Omega \ll \Omega_0$, the effective c.o.m temperature becomes:

$$T_{\text{eff}} = T_0 \frac{\Gamma_0}{\Gamma_0 + \delta\Gamma} \quad (44)$$

with T_0 being the equilibrium c.o.m temperature without feedback ($\delta\Gamma = 0$). It is therefore possible to increase/ decrease the c.o.m temperature by decreasing/ increasing $\delta\Gamma$, respectively. This is done by applying the correct modulation w.r.t the particles

position. The specifics of experimental measurement will not be discussed within this report.

The following is generalised from [36]. After measurement of the particles position, the PSD is found to be:

$$S_{qq}(\Omega) = \gamma^2 \frac{\Gamma_0 k_B T_0 / (\pi m)}{([\Omega_0 + \delta\Omega]^2 - \Omega^2)^2 + \Omega^2 [\Gamma_0 + \delta\Gamma]^2} \quad (45)$$

To fit this with the experimental data, it is measured in nm^2/Hz , however the signal (from QPD) outputs the units V^2/Hz . The γ is a conversion factor from $V \rightarrow \text{nm}$ in units of V/m . Fitting the PSD to a Lorentzian (idealised PSD derived using kinetic theory of gases) results in:

$$S_{qq}^{exp} = \frac{A}{(B^2 - \Omega^2)^2 + \Omega^2 C^2} \quad (46)$$

where

$$\begin{aligned} A &:= \frac{\gamma^2 k_B T_0 \Gamma_0}{\pi m}, \\ B &:= \Omega_0 + \delta\Omega, \\ C &:= \Gamma_0 + \delta\Gamma \end{aligned} \quad (47)$$

are free fit parameters. To find the levitated particles *mass*, the values $\delta\Omega = 0$, $\delta\Gamma = 0$ at $T_0 = 300\text{K}$ (thermal equilibrium at room temperature) are used for the fit to the PSD. To find the levitated particles effective c.o.m *temperature*, the PSD for a particle at thermal equilibrium ($T_0 = 300\text{K}$) is compared with that of the PSD fit to the Lotenzian. The term $\gamma^2 k_B T_0 / \pi m$ is extracted. Using this, the parameters Γ_0 and $\delta\Gamma$ damping terms are extracted from the fit after feedback cooling has occurred. Equation 41 is then used to get the resulting c.o.m temperature. Another important outcome is the *mechanical quality factor*, Q_m . The PSD is once again fit by the Lorentzian and the full width half maximum ($\Delta\Omega$) and mean frequency (Ω_0) are found. $Q_m = \Omega_0 / \Delta\Omega$. If collisions are dominated by those with the background gas, then $Q_m = \Omega_0 / \Gamma_0$. This term is a measure of the energy stored in the harmonic oscillator over the energy dissipated within a single radian oscillation.

Feedback Limits

In the quantum limit, discrete states are separated by energy $\hbar(\Omega_0 + \delta\Omega) \sim \hbar\Omega_0$. The mean thermal occupancy number is given by [14]:

$$\langle n \rangle = \frac{k_B T_{\text{eff}}}{\hbar\Omega_0} = \frac{m\Omega_0^2 \langle q^2 \rangle}{\hbar\Omega_0} \quad (48)$$

The quantum ground state may be achieved when $\langle n \rangle < 1$. For this to be achieved, T_{eff} needs to be very low ($< 10 \mu\text{K}$) and Ω_0 needs to be very high ($> 100 \text{ kHz}$). These extreme values imply a very small damping rate which requires an ultrahigh vacuum ($\sim 10^{-11} \text{ mBar}$) to produce. Other limitations stopping ground state cooling from being achieved include: laser power noise, electrical noise floor, the photon recoil limit, the detector bandwidth and the quantum limit. All of these sources of error limit the lowest attainable temperature T_{eff} .

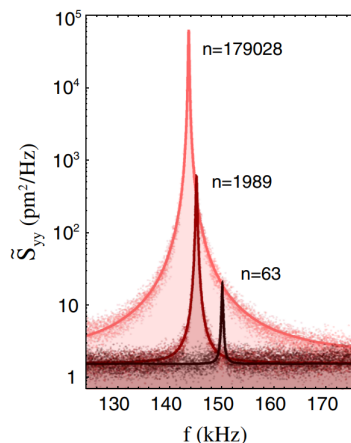


Figure 6: Jain *et al.* were able to reach $n=62.5 \pm 5$ with corresponding $T_0=(450.5 \pm 31.1)\mu\text{K}$. They found that at these low pressures ($2 \times 10^{-8} \text{ mbar}$), the damping rate becomes negligibly small and motion is dominated by photon shot noise. Hence parametric feedback cooling does not work very well below $n \sim 50$. From Ref. [44]

3 Method

Traditional feedback electronics use an analog electric signal to modulate the intensity of the laser by employing an Electro-Optic-Moderator (EOM). The system itself is composed of many separate parts; a bandpass filter (to restrict background frequencies/ frequency shifts), a variable gain amplifier (amplifying signal to mitigate subsequent additive noise), a phase shifter (phase shift required for parametric feedback cooling), a frequency doubler (the output frequency must be twice that of the inputted particle position frequency) and an adder (summing the separate output signals for each d.o.f). These types of setups require complex circuit designs and end up being very specialised, costly and inflexible.

Feedback cooling with rotational optomechanics requires working with much greater frequencies than those with strictly translational motion (as highlighted in section 2.3). As a consequence we require ultra-fast detection and feedback. This can be achieved by using traditional specialised hardware (such as in [27]), but there are other cheaper alternatives. One such solution is the implementation of FPGA based feedback systems. Feedback cooling of nanoparticles using FPGA based devices have been conducted here [51–55]. Some other advantages of using FPGA based digital signal acquisition and processing systems over traditional analog systems include: system may be automated and controlled remotely, direct acquisition of digital data, independence from temperature (analog filters can drift with time and temperature) and greater flexibility (without hardware modification). Some disadvantages include: latencies from analog-digital/ digital-analog conversions, quantization noise, finite bandwidth arising from time discrete processing and finite wordlength effects (leading to round-off errors). These are mitigated by using analog-to-digital and digital-to-analog converters (ADC and DAC) with appropriate sampling rates and by using the correct dynamic conversion range.

3.1 FPGA

An FPGA (Field Programmable Gate Array) is a type of re-programmable logic circuit. A matrix of configurable logic blocks (CLB's) are all connected through programmable interconnects. "Wiring" the CLB's in different configurations allows complex combinational and sequential circuits to be formed, which can then be used to implement different logic functions. This type of logic allows instructions to be executed in parallel, making them much faster than traditional processing systems which execute tasks sequentially. The register-transfer-level (RTL) description is achieved by utilising a hardware description language (HDL). Many FPGA's are also equipped with a separate CPU processing system, which allows for greater flexibility (can execute programs written in normal programming languages) and control. The FPGA used within this report is *STEMlab's* Red Pitaya.

3.2 Red Pitaya

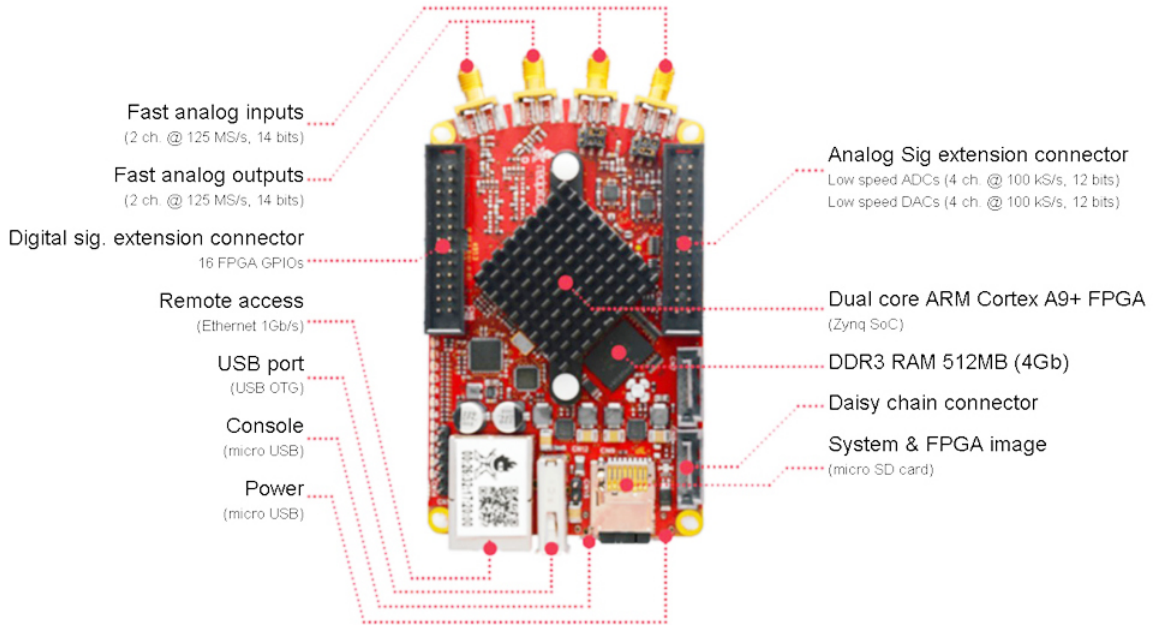


Figure 7: Red Pitaya hardware features. From Ref. [56]

The Red Pitaya (RP) comprises of a Xilinx Zynq-7000 system on chip (SoC) that combines an ARM A9 dual core CPU with an on-chip FPGA [57]. It is equipped with a dual channel ADC and DAC I/O (Input/Output) that have a sample rate of 125 Msps (Mega samples per second) and a resolution of 14 bits [58]. The ADC inputs have a maximum voltage range of $\pm 1V / \pm 20V$ (by adjusting input settings) and the DAC outputs have a maximum voltage range of $\pm 1V$, which might limit some applications (not applicable to this report). The ADC has a latency of 48 ns [59], whilst the DAC has a latency of 43 ns [60]. There is also a high input noise of $\sim 1 \frac{\mu V}{\sqrt{Hz}}$ [58]. The RP CPU runs a Linux based operating system, ensuring that analysis and control algorithms can be run in conjunction with the FPGA implementation. The RP also has a USB port and an ethernet port, allowing data transfer and remote control. These features are highlighted in figure 8. To implement the HDL design onto the RP FPGA, Xilinx's Vivado Design Suite is used. The HDL being used is Verilog. The specifics are highlighted in the next section.

4 Experiment and Protocol

Programming the RP is achieved primarily within the Vivado software environment. This is done by utilising the IP integrator block design. An IP core is a reusable unit of logic (written in a HDL) within the integrated circuit that is specific to the type of hardware being used. Hardware specific embedded block designs are already contained within Vivado and can be added when creating a new project and inputting the board part number. Modules are code written in a HDL that perform logic between set I/O ports. Each port acts as pins (like a chip placed on a PCB) where the module can receive/send signals to other ports from different modules. This is done by using the AXI protocol communication [61]. Custom modules and IP cores can also be instantiated into the block design by using the IP integrator.

The Vivado project flow is as follows:

Create new block design/ import embedded design → Create/ import constraint files → create/ import modules → join all relevant pins/ validate design → run synthesis → run implementation → run simulation → generate bitstream

Once the bitstream file is obtained, it is uploaded onto the RP and executed. For this project, custom RP modules and constraint files from Pavel Demin are used to form the base of the project [62]. The next couple of sections highlight the projects that were most helpful when learning about the RP within the context of levitated nanophysics.

4.1 Red Pitaya High Bandwidth Averager

The fundamentals of programming the RP are covered by Anton Potočník’s mini projects [63]. The most relevant project is that for the High Bandwidth Averager [64]. This project shares several RP specific modules that can be reused for any digital signal processing project, namely the RP ADC, RP DAC and Block memory (BRAM) generator blocks. The block memory generator module is especially important and will be discussed later.

4.2 Red Pitaya PLL

Another project that was important in understanding the use of RP specific modules was by Felix Tebbenjohanns [51]. This project uses the RP for a phase-locked-loop (PLL) implementation for parametric feedback cooling of a levitated nanoparticle. The principle works as follows: The RP’s two RF input/ outputs are used to facilitate two independent PLL’s. This consists of a phase detector (measuring the phase difference between the input signal and an internally generated oscillator), a PI filter to lock the phase and a numerically controlled oscillator (NCO) to create an arbitrary sine output signal.

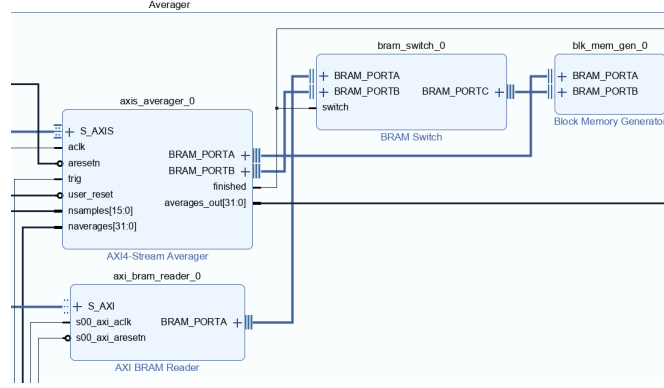


Figure 8: Block memory generator module used in RP High Bandwidth Averager. Files from Ref. [64]

4.3 Our Experiment

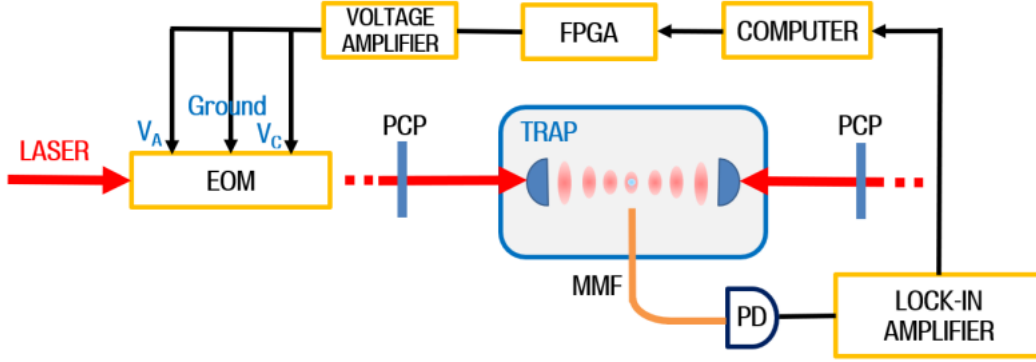


Figure 9: Simplified view of the experiment schematic

Experimental procedure

A 1550 nm TEM_{00} laser is used to create an optical trap at the centre of a vacuum chamber. This is done by using a beam splitter to create two counterpropagating beams (acting as standing waves), with the trapping region in the centre. A silicon nanorod of diameter $d(= 130 \pm 13)$ nm and length $l(= 725 \pm 15)$ nm is trapped in the centre. A 1 mm core multi-mode fibre (MMF) placed close to the trap centre ($< 100\mu\text{m}$), collects scattered light from the trapped nanoparticle, yielding information about the translational and rotational d.o.f. This is connected to a photodetector (PD) which is able to convert the particles positional/ rotational data into an electrical signal. This data is then fed into a lock-in amplifier - a phase-locked-loop (PLL) that generates an output voltage with appropriate phase for parametric feedback cooling. This is only done for a single direction (along \hat{z}). To accomplish this in three dimensions the setup will need to be repeated along \hat{x} and \hat{y} , each with their own PLL's to calculate the the respective phase shift. The PLL being used is the Zurich Instruments HF2PLL [65]. Next the posi-

tional data and phase shift are recorded on a computer, before the voltage is transmitted to the RP. The RP performs some fast data processing and outputs two analog signals.

The outputs of the RP are in the form of two voltages; V_A and V_C . These voltages correspond to different settings of the electro-optic modulator (EOM) - which in turn controls settings on the polarization control paddle (PCP) to adjust the polarization of the incident laser beam. The PCP being used is from ThorLabs [66]. These PCP's incorporate a half-wave plate between two quarter-wave plates. By using this configuration, linear, circular and elliptical polarization states may be achieved. PCP's are placed at both directions of the trapping zone to control all incident laser polarization.

The values for V_A and V_C are calibrated by increasing the output PLL voltage, V , incrementally and measuring the corresponding polarization angle. This is seen for the half-wave plate in figure 11. These voltages are outputted into a voltage amplifier before being inputted into the EOM. The EOM is also able to modulate the intensity of the trapping laser (through direct input of the PLL signal) to cool the translational motion of the trapped particle.

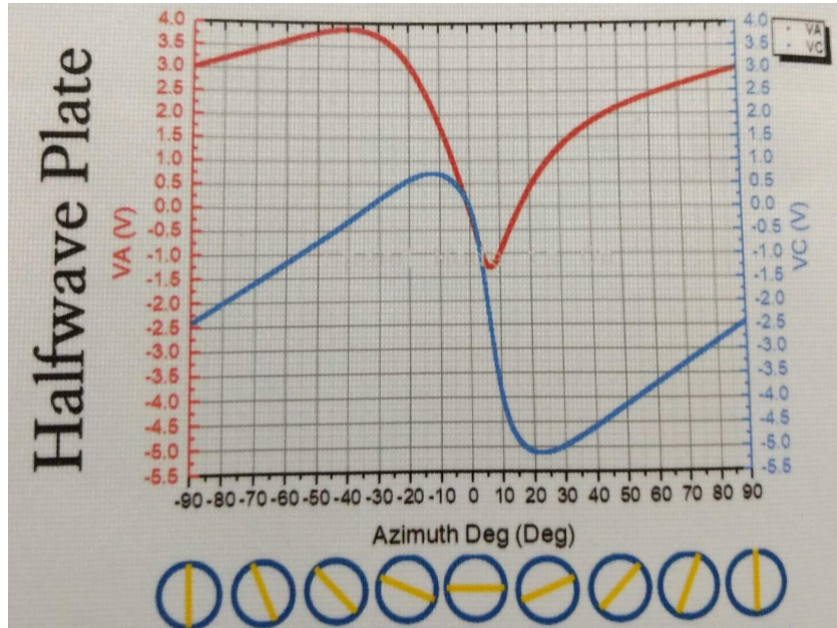


Figure 10: Values of V_A and V_C calculated with a half-wave plate

Feedback cooling procedure

Translational parametric feedback cooling is achieved by modulating the intensity of the trapping laser (as highlighted in section 2.4). The outputted PLL signal is sent directly to the EOM, which is able to control the trapping lasers intensity and cool the translational d.o.f (x, y, z) of the trapped nanorod's c.o.m motion.

Polarisation parametric feedback cooling is achieved by using the RP's outputted V_A and V_C voltage signals. When the laser is circularly polarized, the interaction between scattered light produces a torque (as highlighted in section 2.3) that forces the particle in the plane orthogonal to the beam axis, while it's c.o.m motion remains trapped due to translational feedback cooling. The polarization response cools the rotational d.o.f (α and β).

Red Pitaya Programming protocol

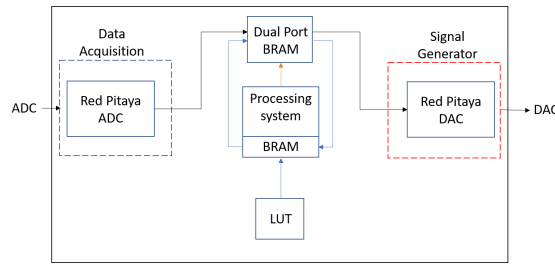


Figure 11: Simplified Block Diagram of the FPGA implementation

The PLL output signal, V , is inputted through one of the RP's 14 bit ADC channels. A *Data Acquisition* hierarchy, housing a RP ADC module receives the data and sends it to an input on the Dual Port BRAM module. This is achieved through an AXI stream protocol and is able to interface with the processing system through an AXI interconnect (not shown in simplified diagram) [61]. The *LUT* hierarchy instantiates the pre-calibrated values of V , V_A and V_C into the BRAM. The *Dual Port BRAM module* takes the inputted V signal and finds the corresponding V_A and V_C values within the BRAM. This is sent to the *Signal Generator* hierarchy which houses a RP DAC module - that is able to output the data directly to the two RP 14 bit DAC channels.

The values of the output PLL signal, V , and V_A , V_C signals are calibrated and stored on a look-up-table (LUT). This data can be instantiated into the block memory (BRAM) of the red pitaya for fast access (compared Direct-RAM). BRAM stands for Block Random Access Memory and is used for storing large amounts of data within an FPGA. Our specific RP model (STEMlab 125-14 with Xilinx part XC7Z010-1CLG400C) contains 60 36 Kb blocks (of BRAM) which corresponds to 2.1 Mb of storage [57]. BRAM comes in a finite size (4.8/16/32 kb) and can have custom width and depth - our BRAM configuration is 32 wide by 1024 depth. The tool used to instantiate the LUT into the BRAM is Data2MEM [67]. Data2MEM is able to store contiguous blocks of data across multiple BRAM's. The LUT can either be stored as a single array or each column may be stored separately. Below is an example of how data is stored in a 64 bit BRAM address space.

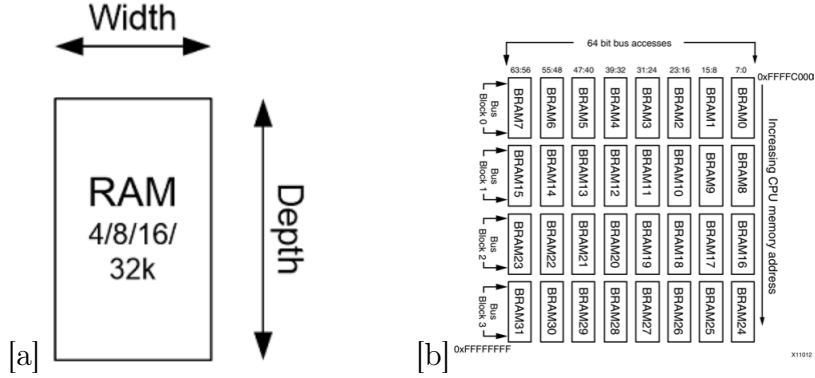


Figure 12: [a] The width and depth of a single block ram can be customised for any specific application. From Ref. [68] [b] 64 bit BRAM address space. From Ref. [67]

An address bus contains information about where data is stored in the physical memory and allows communication through read/ write commands. The address space is defined by the upper right and lower left corners. Each byte of data is stored as follows: Byte 0 is stored within the first byte location of of BRAM 7, byte 1 into the first byte location of BRAM 6 and so on. Looping around, byte 8 is stored within the second byte location of BRAM7 and the process is repeated until the entire memory space is filled.

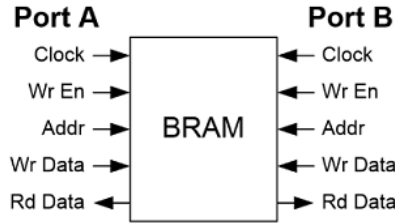


Figure 13: A Dual Port BRAM configuration. From Ref. [68]

Now that the voltage LUT has been instantiated into the BRAM, a mechanism by which any input voltage is converter into the corresponding V_A and V_C must be found. This can be achieved by using a dual port BRAM configuration (as seen in Anton Potočník's project in section 4.1). The module (seen in figure 13) has two sides - Ports A and B. Both of these have an input for a system clock speed. Our system is run at ~ 10 MHz, this is achieved by using a clock divider module to reduce the original clock speed of 125 MHz from the processing system. Data is read/ written on the positive edge of each clock cycle at the address specified by *Addr*. These are the same BRAM address busses as discussed earlier. Reading/ writting stops once *Wr En* has been engaged. Written data is inputted with *Wr Data* and read values are outputted with *Rd Data*. The dual port configuration allows reading and writting on the same clock cycle. So the mechanism works as follows: The input voltage, V , is written into a location within the BRAM at port A. An algorithm (within the dual port BRAM) looks up the corresponding V_A and V_C from the LUT that was instantiated before. The address bus is located and the data

is outputted at port B. One way of producing a dual port BRAM module is through Vivado’s block memory generator IP core.

4.4 Expected Results and Analysis

Unfortunately, programming of the Red Pitaya could not be completed to obtain any meaningful results. A protocol has been provided to produce two of the main components within the project file. Had the project been successful, the output would have been the production of output signals corresponding to the V_A and V_C output voltages. Following the Vivado project flow, a simulation test bench could have been run and an analysis (see [69]) on the results conducted. An example of a simulation run has been provided in figure 14. The main source of error in this project is the RP high input noise ($\sim 1 \frac{\mu V}{\sqrt{Hz}}$ [58]). This is especially high when compared with the input noise of the PLL ($5 \frac{nV}{\sqrt{Hz}}$ [65]). There are also some latency errors arising from the ADC (48 ns [59]) and DAC (43 ns [60]). Although these are considered insignificant as the system is running at $\sim 10 MHz$ ($\sim 1 \times 10^{-6}s$). However it should be noted that these processing latencies may lead to group delay between the input and output signals. The consequent phase response may develop linear frequency dependencies which limits the effective bandwidth of the feedback system. For a group delay of $\tau_g=91$ ns, there is a frequency dependent phase response [70]:

$$\frac{d\phi}{d\nu} = -\tau_g 360 \approx \frac{33^\circ}{MHz} \quad (49)$$

Errors from other sources must also be considered. Inherent errors from the experiment have briefly been discussed in *feedback limits*. The electrical noise floor can be lowered by changing the PLL amplifier with a lower noise version. Doing so will allow the feedback mechanism to reach lower c.o.m temperatures (as PSD will have greater resolution). Another way to decrease electrical noise is by increasing the signal to noise ratio (SNR), this can be achieved by placing a low noise voltage amplifier after the detector [36]. As a consequence of all inherent equipment noise, the RP’s feedback scheme may create a positive feedback loop such that the feedback signal grows without bound until the RP’s output limit has been reached. This is referred to as *parasitic feedback* and has been documented before in feedback cooling [52].

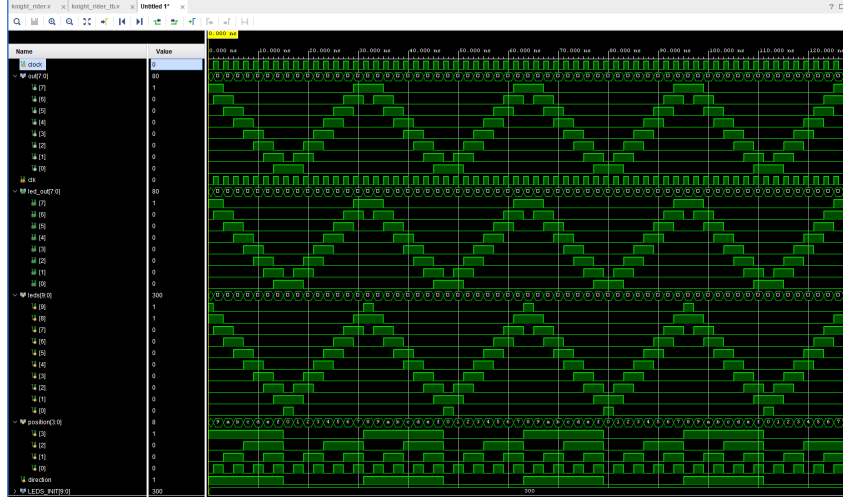


Figure 14: Example of a simulation run. It ensures that the synthesized or implemented design meets functional requirements and behaves as expected. Files from Ref. [63].

5 Summary and Outlook

Although no formal results have been obtained, a protocol has been provided to allow the theoretical completion of this project. The shortcomings in programming the RP is attributed to a lack of experience and in difficulty with finding adequate resources online. In particular, there were difficulties with instantiating the LUT in the BRAM. Since this required a custom module to be written, finding similar code online was challenging. Most projects working with FPGA feedback cooling employ the use of variable phase shifts to provide the feedback signal [52, 70]. Such schemes are easily realisable since they work with IP cores already available within Vivado.

A short analysis on the contributions of error within the experiment has been conducted and their consequences discussed. The aim of the project was to demonstrate that the RP could be used as a suitable feedback electronic to cool rotational degrees of freedom through polarisation feedback. To this effect, it would be beneficial to compare the RP to "traditional" feedback electronics that it would be replacing. This type of comparison has been done before by comparing the PLL amplifier to a RP PLL application [51].

The RP can also be used to perform a measurement of the voltage noise density within the entire circuit [71]. By doing so, the noise floor of the RP can be found and compared to other components in the circuit. For example:

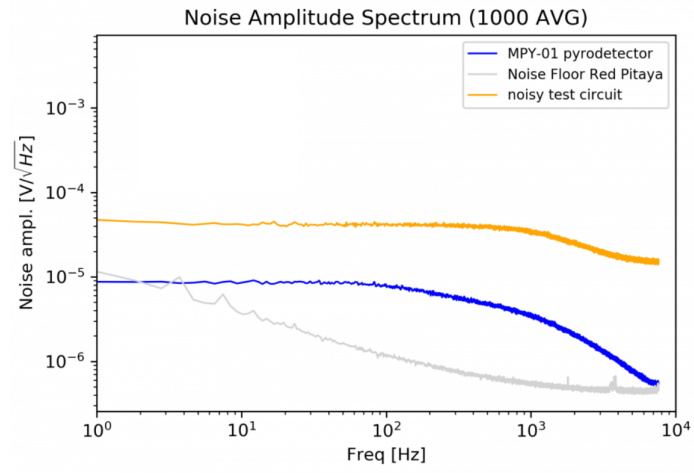


Figure 15: The RP noise floor is seen in grey. The connected circuits noise is in yellow. An expensive FFT-Analyzer is used to perform the same measurement and is found to be within error of the ADC. From Ref. [71]

A Appendix

A.1 Corrections to Polarizability

After accounting for radiative losses, the *effective* polarizability is given as [29, p. 278]:

$$\alpha_{eff}(\omega) = \frac{\alpha(\omega)}{1 - i\frac{k^3}{6\pi\epsilon_0}\alpha(\omega)} \approx \alpha(\omega) + i\frac{k^3}{6\pi\epsilon_0}\alpha^2(\omega) \quad (50)$$

A.2 Gaussian Paraxial Approximation

Paraxial approximation of optical fields: (From Ref. [29, p. 47])

For an optical wave propagating along the z-axis, there is dispersal in the transverse directions. For the wavevector $\mathbf{k} = (k_x, k_y, k_z)$, the transverse components (k_x, k_y) are small compared to k and k_z may be expanded as:

$$k_z = k\sqrt{1 - (k_x^2 + k_y^2)/k^2} \approx k - \frac{k_x^2 + k_y^2}{2k} \quad (51)$$

A.3 Beam Power

The power of the laser (used in equation 14) is given by the following equation [36]:

$$P(r_{app}, z) = P_0 \left[1 - e^{\frac{-2r_{app}^2}{W(z)^2}} \right] \quad (52)$$

where r_{app} is the radius of the aperture in the x,y plane and P_0 is the total power transmitted:

$$P_0 = \frac{1}{2}\pi I_0 W_0^2 \quad (53)$$

A.4 Exact field distribution

The exact field distribution is found by accounting for all plane waves at the focus, expressed through an angular spectrum representation. The Debye integral [29]:

$$\mathbf{E}(\rho, \varphi, z) = \frac{ikf e^{-ikf}}{2\pi} \int_0^{\theta_{\max}} \int_0^{2\pi} \mathbf{E}_{\infty}(\theta, \phi) e^{ikz \cos \theta} e^{ik\rho \sin \theta \cos(\phi - \varphi)} \sin \theta d\phi d\theta, \quad (54)$$

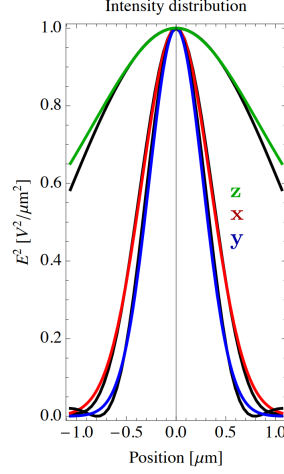


Figure 16: Differences between the Debye integral (black) and the Gaussian approximation (coloured according to axis). The difference arises as the Gaussian approximation does not account for diffraction. At $\lambda/2$ away from the origin, the model fits very well. From Ref. [14]

A.5 Photon shot noise

Damping rate from the Photon shot noise [44] leads to a damping rate [42]:

$$\Gamma_{\text{rad}} = \frac{c_{\text{dp}} P_{\text{scat}}}{M c^2} \quad (55)$$

where the factor c_{dp} is dependent on the particles relative motion to the polarization of light ($=2/5$ for parallel, $4/5$ for perpendicular) and P_{scat} is the power of the scattered light. $\Gamma_{\text{rad}} \ll \Gamma_{\text{gas}}$ upto $P_{\text{gas}} \sim 10^{-6}$ mbar [41].

A.6 A brief summary of Internal Temperature

The following definitions are from [41]. Background gas (impinging gas) collides with the trapped particle, sticking to it's hot surface for some time and then ejecting (emitted gas) to a region of high intensity (through photophoresis). This process is called accommodation and there is energy exchange characterized by the energy accommodation coefficient (fraction of thermal energy removed by collision):

$$\alpha_{\text{C}} = \frac{T_{\text{em}} - T_{\text{im}}}{T_{\text{int}} - T_{\text{im}}} \quad (56)$$

where T_{em} is the temperature of the emitted gas, T_{im} is the temperature of the impinging gas and T_{int} is the internal temperature of the levitated particle. Within the Knudsen regime, T_{im} equalises with the T_{env} environmental temperature such that the

effective c.o.m temperature becomes:

$$T_0 = \frac{T_{im}\Gamma_{im} + T_{em}\Gamma_{em}}{\Gamma_{tot}} \quad (57)$$

where $\Gamma_{tot} = \Gamma_{im} + \Gamma_{em}$ and $\Gamma_{em} = \frac{\pi}{8}\Gamma_{im}\sqrt{T_{em}/T_{im}}$.

A.7 Red Pitaya project

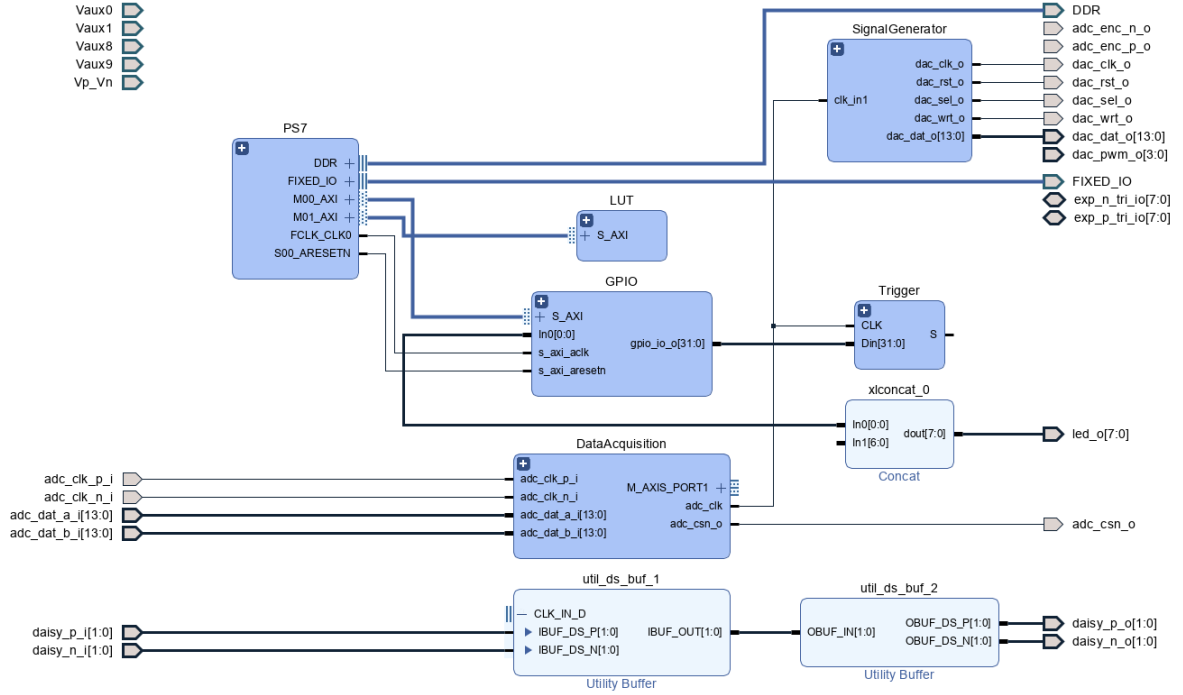


Figure 17: Overview of Block Design

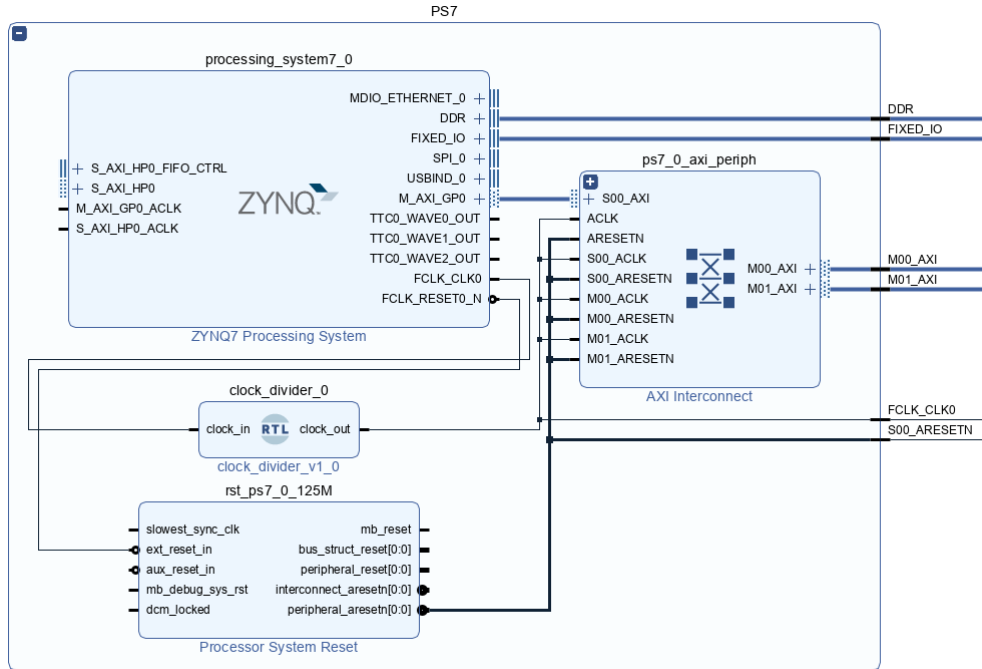


Figure 18: Processing system Hierarchy

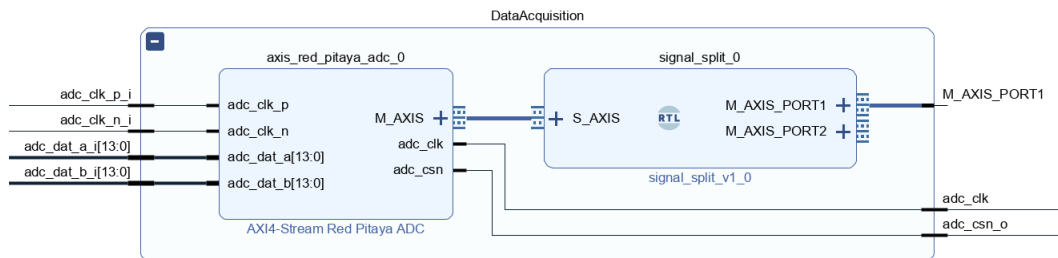


Figure 19: Data Acquisition Hierarchy

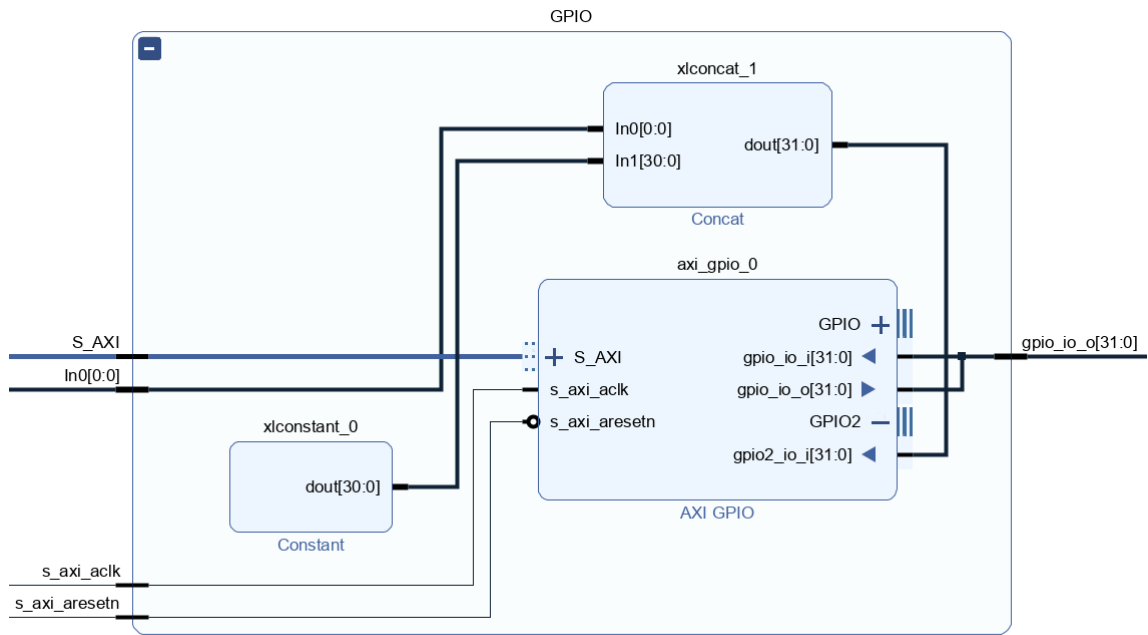


Figure 20: GPIO Hierarchy

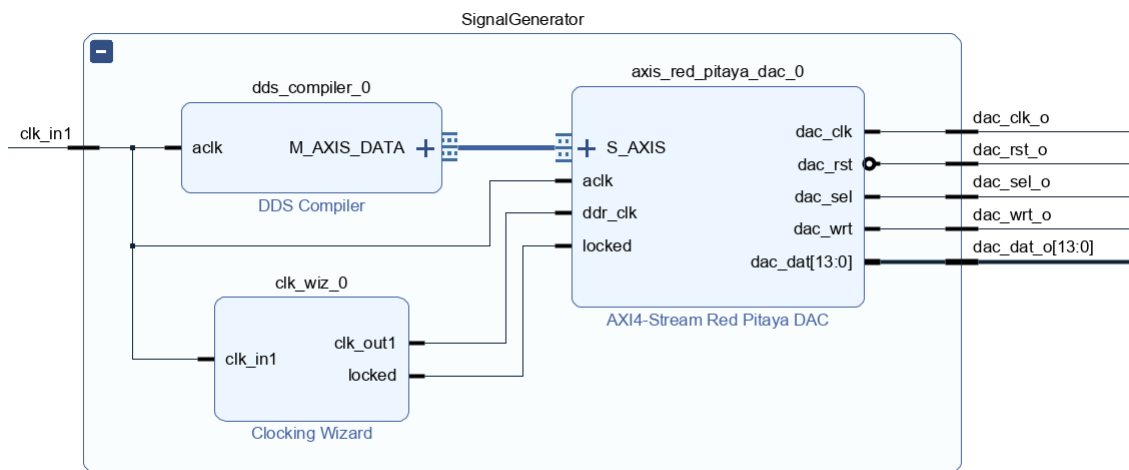


Figure 21: Signal Generator Hierarchy

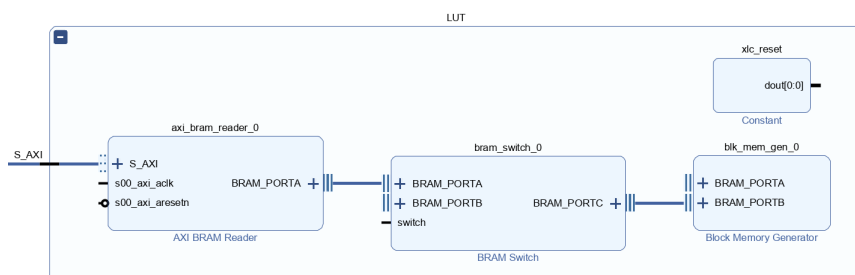


Figure 22: Look-up-table Hierarchy

References

- [1] A. Ashkin. “Acceleration and Trapping of Particles by Radiation Pressure”. In: *Physical Review Letters* 24 (4 1970). ISSN: 00319007. DOI: 10.1103/PhysRevLett.24.156.
- [2] A. Ashkin and J. M. Dziedzic. “Stability of optical levitation by radiation pressure”. In: *Applied Physics Letters* 24 (12 1974). ISSN: 00036951. DOI: 10.1063/1.1655064.
- [3] A. Ashkin and J. M. Dziedzic. “Optical levitation in high vacuum”. In: *Applied Physics Letters* 28 (6 1976). ISSN: 00036951. DOI: 10.1063/1.88748.
- [4] A. Ashkin and J. M. Dziedzic. “Feedback stabilization of optically levitated particles”. In: *Applied Physics Letters* 30 (4 1977). ISSN: 00036951. DOI: 10.1063/1.89335.
- [5] Scot C. Kuo and Michael P. Sheetz. *Optical tweezers in cell biology*. 1992. DOI: 10.1016/0962-8924(92)90016-G.
- [6] Karel Svoboda and Steven M. Block. *Biological applications of optical forces*. 1994. DOI: 10.1146/annurev.bb.23.060194.001335.
- [7] Keir C. Neuman and Attila Nagy. *Single-molecule force spectroscopy: Optical tweezers, magnetic tweezers and atomic force microscopy*. 2008. DOI: 10.1038/nmeth.1218.
- [8] Thomas T. Perkins. “Optical traps for single molecule biophysics: A primer”. In: *Laser and Photonics Reviews* 3 (1-2 2009). ISSN: 18638880. DOI: 10.1002/lpor.200810014.
- [9] Praveen C. Ashok and Kishan Dholakia. *Optical trapping for analytical biotechnology*. 2012. DOI: 10.1016/j.copbio.2011.11.011.
- [10] Steven Chu. “Laser manipulation of atoms and particles”. In: *Science* 253 (5022 1991). ISSN: 00368075. DOI: 10.1126/science.253.5022.861.
- [11] Rudolf Grimm, Matthias Weidemüller, and Yurii B. Ovchinnikov. “Optical Dipole Traps for Neutral Atoms”. In: *Advances in Atomic, Molecular and Optical Physics* 42 (C 2000). ISSN: 1049250X. DOI: 10.1016/S1049-250X(08)60186-X.
- [12] Tongcang Li et al. “Measurement of the instantaneous velocity of a brownian particle”. In: *Science* 328 (5986 2010). ISSN: 00368075. DOI: 10.1126/science.1189403.
- [13] Tongcang Li, Simon Kheifets, and Mark G. Raizen. “Millikelvin cooling of an optically trapped microsphere in vacuum”. In: *Nature Physics* 7 (7 2011). ISSN: 17452481. DOI: 10.1038/nphys1952.
- [14] Jan Gieseler. “Dynamics of optically levitated nanoparticles in high vacuum”. PhD thesis. The Institute of Photonic Sciences, 2014.

- [15] Arthur La Porta and Michelle D. Wang. “Optical torque wrench: angular trapping, rotation, and torque detection of quartz microparticles”. In: *Physical review letters* 92 (19 2004). ISSN: 00319007.
- [16] Alexis I. Bishop et al. “Optical microrheology using rotating laser-trapped particles”. In: *Physical review letters* 92 (19 2004). ISSN: 00319007.
- [17] M. Bhattacharya and P. Meystre. “Using a Laguerre-Gaussian beam to trap and cool the rotational motion of a mirror”. In: *Physical Review Letters* 99 (15 2007). ISSN: 00319007. DOI: 10.1103/PhysRevLett.99.153603.
- [18] Yoshihiko Arita, Michael Mazilu, and Kishan Dholakia. “Laser-induced rotation and cooling of a trapped microgyroscope in vacuum”. In: *Nature Communications* 4 (2013). ISSN: 20411723. DOI: 10.1038/ncomms3374.
- [19] Jasper Chan et al. “Laser cooling of a nanomechanical oscillator into its quantum ground state”. In: *Nature* 478 (7367 2011). ISSN: 00280836. DOI: 10.1038/nature10461.
- [20] A. D. O’Connell et al. “Quantum ground state and single-phonon control of a mechanical resonator”. In: *Nature* 464 (7289 2010). ISSN: 00280836. DOI: 10.1038/nature08967.
- [21] P. F. Barker. “Doppler cooling a microsphere”. In: *Physical Review Letters* 105 (7 2010). ISSN: 00319007. DOI: 10.1103/PhysRevLett.105.073002.
- [22] Simon Gröblacher et al. “Demonstration of an ultracold micro-optomechanical oscillator in a cryogenic cavity”. In: *Nature Physics* 5 (7 2009). ISSN: 17452481. DOI: 10.1038/nphys1301.
- [23] I. Wilson-Rae et al. “Theory of ground state cooling of a mechanical oscillator using dynamical backaction”. In: *Physical Review Letters* 99 (9 2007). ISSN: 00319007. DOI: 10.1103/PhysRevLett.99.093901.
- [24] Gambhir Ranjit et al. “Zeptonewton force sensing with nanospheres in an optical lattice”. In: *Physical Review A* 93 (5 2016). ISSN: 24699934. DOI: 10.1103/PhysRevA.93.053801.
- [25] Stefan Kuhn et al. “Cavity-Assisted Manipulation of Freely Rotating Silicon Nanorods in High Vacuum”. In: *Nano Letters* 15 (8 2015). ISSN: 15306992. DOI: 10.1021/acs.nanolett.5b02302.
- [26] Benjamin A. Stickler et al. “Rotational cavity cooling of dielectric rods and disks”. In: *Physical Review A* 94 (3 2016). ISSN: 24699934. DOI: 10.1103/PhysRevA.94.033818.
- [27] Stefan Kuhn et al. “Full rotational control of levitated silicon nanorods”. In: *Optica* 4 (3 2017). ISSN: 2334-2536. DOI: 10.1364/optica.4.000356.

- [28] Stefan Kuhn et al. “Optically driven ultra-stable nanomechanical rotor”. In: *Nature Communications* 8 (1 2017). ISSN: 20411723. DOI: 10.1038/s41467-017-01902-9.
- [29] Lukas Novotny and Bert Hecht. *Principles of nano-optics*. Vol. 9781107005464. 2009. DOI: 10.1017/CB09780511794193.
- [30] David S. Bradshaw and David L. Andrews. “Manipulating particles with light: Radiation and gradient forces”. In: *European Journal of Physics* 38 (3 2017). ISSN: 13616404. DOI: 10.1088/1361-6404/aa6050.
- [31] Silvia Albaladejo et al. “Scattering forces from the curl of the spin angular momentum of a light field”. In: *Physical Review Letters* 102 (11 2009). ISSN: 00319007. DOI: 10.1103/PhysRevLett.102.113602.
- [32] S. P. Tarafdar and M. S. Vardya. “The Rayleigh Scattering Cross-Sections of He, C, N and O”. In: *Monthly Notices of the Royal Astronomical Society* 145 (2 1969). ISSN: 0035-8711. DOI: 10.1093/mnras/145.2.171.
- [33] A. Ashkin and J. M. Dziedzic. “Optical Levitation by Radiation Pressure”. In: *Applied Physics Letters* 19.8 (Oct. 1971), pp. 283–285. DOI: 10.1063/1.1653919.
- [34] A. Ashkin. “Acceleration and Trapping of Particles by Radiation Pressure”. In: *Phys. Rev. Lett.* 24 (4 Jan. 1970), pp. 156–159. DOI: 10.1103/PhysRevLett.24.156.
- [35] P. Zemánek et al. “Optical trapping of Rayleigh particles using a Gaussian standing wave”. In: *Optics Communications* 151 (4-6 1998). ISSN: 00304018. DOI: 10.1016/S0030-4018(98)00093-5.
- [36] Jamie Vovrosh. “Parametric feedback cooling and squeezing of optically levitated particles”. PhD thesis. University of Southampton, 2018.
- [37] Erik Hebestreit. “Thermal Properties of Levitated Nanoparticles”. PhD thesis. ETH Zürich, 2017.
- [38] Jan Gieseler, Lukas Novotny, and Romain Quidant. “Thermal nonlinearities in a nanomechanical oscillator”. In: *Nature Physics* 9 (12 2013). ISSN: 17452481. DOI: 10.1038/nphys2798.
- [39] Jan Gieseler et al. “Dynamic relaxation of a levitated nanoparticle from a non-equilibrium steady state”. In: *Nature Nanotechnology* 9 (5 2014). ISSN: 17483395. DOI: 10.1038/nnano.2014.40.
- [40] Jan Gieseler et al. “Nonlinear mode coupling and synchronization of a vacuum-trapped nanoparticle”. In: *Physical Review Letters* 112 (10 2014). ISSN: 10797114. DOI: 10.1103/PhysRevLett.112.103603.
- [41] James Millen et al. *Optomechanics with levitated particles*. 2020. DOI: 10.1088/1361-6633/ab6100.

- [42] James Millen and Jan Gieseler. “Single Particle Thermodynamics with Levitated Nanoparticles”. In: *Thermodynamics in the Quantum Regime: Fundamental Aspects and New Directions*. Ed. by Felix Binder et al. Cham: Springer International Publishing, 2018, pp. 853–885. ISBN: 978-3-319-99046-0. DOI: 10.1007/978-3-319-99046-0_35.
- [43] S. A. Beresnev, V. G. Chernyak, and G. A. Fomyagin. “Motion of a spherical particle in a rarefied gas. Part 2. Drag and thermal polarization”. In: *Journal of Fluid Mechanics* 219 (1990). ISSN: 14697645. DOI: 10.1017/S0022112090003007.
- [44] Vijay Jain et al. “Direct Measurement of Photon Recoil from a Levitated Nanoparticle”. In: *Physical Review Letters* 116 (24 2016). ISSN: 10797114. DOI: 10.1103/PhysRevLett.116.243601.
- [45] Thai M. Hoang et al. “Torsional Optomechanics of a Levitated Nonspherical Nanoparticle”. In: *Physical Review Letters* 117 (12 2016). ISSN: 10797114. DOI: 10.1103/PhysRevLett.117.123604.
- [46] H Shi and M Bhattacharya. “Optomechanics based on angular momentum exchange between light and matter”. In: *Journal of Physics B: Atomic, Molecular and Optical Physics* 49 (15 2016). ISSN: 0953-4075. DOI: 10.1088/0953-4075/49/15/153001.
- [47] Stefan Kuhn et al. *Supplement 1: Full rotational control of levitated silicon nanorods*. Apr. 2017. DOI: 10.1364/OPTICA.4.000356.s001.
- [48] R. Schiffer and K. O. Thielheim. “Light scattering by dielectric needles and disks”. In: *Journal of Applied Physics* 50 (4 1979). ISSN: 00218979. DOI: 10.1063/1.326257.
- [49] J. Millen et al. “Cavity cooling a single charged levitated nanosphere”. In: *Physical Review Letters* 114 (12 2015). ISSN: 10797114. DOI: 10.1103/PhysRevLett.114.123602.
- [50] Jan Gieseler et al. “Subkelvin parametric feedback cooling of a laser-trapped nanoparticle”. In: *Physical Review Letters* 109 (10 2012). ISSN: 00319007. DOI: 10.1103/PhysRevLett.109.103603.
- [51] Felix Tebbenjohanns. *Red Pitaya PLL*. <https://git.ee.ethz.ch/tefelix/redpitayapll>. [Online; accessed 08/04/2021]. 2018.
- [52] Joonas Nätkinniemi. “Optical feedback cooling of a mechanical silicon oscillator with a single laser”. MA thesis. Department of Physics University of Jyväskylä, 2020.
- [53] Luca Ferialdi et al. “Optimal control for feedback cooling in cavityless levitated optomechanics”. In: *New Journal of Physics* 21 (7 2019). ISSN: 13672630. DOI: 10.1088/1367-2630/ab2b69.

- [54] Gerard P. Conangla et al. "Optimal Feedback Cooling of a Charged Levitated Nanoparticle with Adaptive Control". In: *Physical Review Letters* 122 (22 2019). ISSN: 10797114. DOI: 10.1103/PhysRevLett.122.223602.
- [55] Jiawei Liao et al. "FPGA Implementation of a Kalman-Based Motion Estimator for Levitated Nanoparticles". In: *IEEE Transactions on Instrumentation and Measurement* 68 (7 2019). ISSN: 00189456. DOI: 10.1109/TIM.2018.2879146.
- [56] "FPGA RED". *Labelled diagram of the Red Pitaya*. <https://www.fpga.red/RedPitaya-Ressources.jpg>. [Online; accessed 08/04/2021]. 2021.
- [57] XILINX. *Zynq-7000 SoC Data Sheet*. https://www.xilinx.com/support/documentation/data_sheets/ds190-Zynq-7000-Overview.pdf. [Online; accessed 08/04/2021]. 2018.
- [58] STEMLabs Red Pitaya. *I/O Specifications*. <https://redpitaya.readthedocs.io/en/latest/developerGuide/125-14/fastIO.html#>. [Online; accessed 08/04/2021]. 2021.
- [59] LTC2145-14 Datasheet. *Analog Devices*. <https://www.analog.com/media/en/technical-documentation/data-sheets/21454314fa.pdf>. [Online; accessed 08/04/2021]. 2017.
- [60] DAC1401D125 Datasheet. *Integrated Device Technology*. <https://www.renesas.com/eu/en/document/dst/dac1401d125-datasheet>. [Online; accessed 08/04/2021]. 2012.
- [61] XILINX. *AXI Reference Guide*. https://www.xilinx.com/support/documentation/ip_documentation/axi_ref_guide/v13_4/ug761_axi_reference_guide.pdf. [Online; accessed 08/04/2021]. 2012.
- [62] Pavel Demin. *Red Pitaya Notes*. <https://github.com/pavel-demin/red-pitaya-notes>. [Online; accessed 08/04/2021]. 2021.
- [63] Anton Potočník. *Red Pitaya FPGA Programming Projects*. <http://antonpotocnik.com/?cat=29>. [Online; accessed 08/04/2021]. 2021.
- [64] Anton Potočník. *Red Pitaya FPGA Project 5 – High-Bandwidth Averager*. <http://antonpotocnik.com/?p=514765>. [Online; accessed 08/04/2021]. 2021.
- [65] Zurich Instruments. *HF2PLL Phase-locked Loop leaflet*. https://www.zhinst.com/sites/default/files/documents/2020-01/zi_hf2pll_leaflet_0.pdf. [Online; accessed 08/04/2021]. 2018.
- [66] ThorLabs. *Manual Fiber Polarization Controllers*. https://www.thorlabs.com/newgrouppage9.cfm?objectgroup_id=343. [Online; accessed 08/04/2021]. 2018.
- [67] XILINX. *Data2MEM User Guide*. https://www.xilinx.com/support/documentation/sw_manuals/xilinx11/data2mem.pdf. [Online; accessed 08/04/2021]. 2009.

- [68] NandLand. *NandLand BRAM tutorial*. <https://www.nandland.com/articles/what-is-a-fifo-fpga.html>. [Online; accessed 08/04/2021]. 2018.
- [69] XILINX. *Logic Simulation*. https://www.xilinx.com/support/documentation/sw_manuals/xilinx2016_1/ug937-vivado-design-suite-simulation-tutorial.pdf. [Online; accessed 08/04/2021]. 2016.
- [70] Jost Herkenhoff. “Development of a Digital Feedback System for Advanced Ion Manipulation Techniques within a Penning Trap”. Bachelor’s Thesis. Bremen City University of Applied Sciences, 2020.
- [71] WiredSense. *Measurement of voltage noise density with a Red Pitaya*. <https://www.wiredsense.com/tutorial/measurement-of-voltage-noise-density-with-a-red-pitaya>. [Online; accessed 08/04/2021]. 2021.